13th International Symposium on Turbulence and Shear Flow Phenomena (TSFP13)
Montreal, Canada, June 25–28, 2024

TRANSITION TO TURBULENCE OF AN INCOMPRESSIBLE FLOW OVER A HIGH-LIFT AIRFOIL

Ming Teng
Department of Mechanical Engineering
University of Ottawa
Ottawa, ON K1N 6N5
Ming.Teng@uottawa.ca

Catherine Mavriplis
Department of Mechanical Engineering
University of Ottawa
Ottawa, ON K1N 6N5
Catherine.Mavriplis@uottawa.ca

Abstract

The present study explores the transition to turbulence of an incompressible flow over an airfoil in a high-lift configuration. The focus of the current work is placed on three low chordwise Reynolds numbers: $Re_c = 0.832 \times 10^4$, 1.270×10^4 and 1.830×10^4. The angle of attack stays at 4.0 degrees in all cases. A series of well-resolved three-dimensional direct numerical simulations is implemented via a high-order spectral element method. Results achieve good agreement with existing experimental data, including the observation of characteristic coherent structures. The present work focuses on a quantitative analysis through mean statistics, but also monitors the evolution of instantaneous coherent structures. Evaluations of Reynolds stresses and the turbulent kinetic energy budget are employed to describe the transitional flow behaviour for the cases considered.

Introduction

The flow around an airfoil geometry leads to complex physical phenomena. Beyond examining these intricate mechanisms, research is also motivated by a broad spectrum of practical applications, for example in transportation through the design of efficient aircraft and in energy through the development of wind turbines. The majority of the works for flow over airfoils, either experiments or simulations, focuses on single-element airfoils with a $Re_c \sim O(10^6)$ ($Re_c = U_\infty c/\nu$ denotes chordwise Reynolds number; U_∞ and c represent the freestream velocity and the stowed chord length of the airfoil, respectively; ν is kinematic viscosity), whereas investigations on multi-element configurations are, in comparison, highly limited. Most of these investigations are at high Reynolds numbers, $Re_c \sim O(10^6)$, and on the numerical side they all employ turbulence models. This work is aimed at Direct Numerical Simulation of flow past a multi-element airfoil.

Wang *et al.* (2018) explored the coherent flow structures of an incompressible flow past the 30P30N high-lift airfoil at $Re_c = 0.832 \times 10^4$ and $\alpha = 0 - 16^\circ$ (α signifies the angle of attack) in an experimental setting. Regular longitudinal counter-rotating vortices were observed over the leading edge of the main element when $2.0^\circ \leq \alpha \leq 12.0^\circ$. These structures were conjectured to be Görtler vortices yielded by the shear layer emanating from the slat cove. Wang *et al.* (2019) extended the effort and focused on the Reynolds-number effect on the flow structures over the main element with $\alpha = 4.0^\circ$; Re_c ranged from 0.93×10^4 to 3.05×10^4. A critical Re_c range was identified between $Re_c = 1.27 \times 10^4 - 1.38 \times 10^4$. When Re_c exceeded this range, spanwise vortices started to occur, coexisting with the conjectured Görtler vortices that once dominated the slat wake alone. Such modifications to the flow structures were linked to the flow motions at the slat cusp. Wang & Wang (2021*a*) further investigated this phenomenon and focused on the flow behaviour within the the slat cove at a wide range of Re_c ($0.93 \times 10^4 - 5.20 \times 10^4$) at $\alpha = 4.0^\circ$. Three types of vortex dynamics were identified, depending on the Re_c. Each described a unique interaction between shed vortices from the slat cusp and the flow field near the slat trailing edge. A recent work by Wang & Wang (2021*b*) explored the transition triggered by the slat wake. In this study, Re_c ranged from 1.38×10^4 to 3.05×10^4 with $\alpha = 4.0^\circ$. Instability mechanisms were discussed along with the qualitative description of the transiton routes.

In the low-Reynolds-number range, the boundary layer over the airfoil cannot withstand the severe adverse pressure formed over the main element. This leads to the formation of a separation bubble, to the detriment of airfoil performance (Lissaman, 1983). Yarusevych *et al.* (2006, 2009) experimentally examined the coherent structures in the separated shear layer and wake region of an airfoil (NACA 0025). A low-Reynolds-number range ($5.5 \times 10^4 \leq Re_c \leq 2.1 \times 10^5$) was considered at three angles of attack: $\alpha = 0.0^\circ$, 5.0° and 10.0°, respectively. Scenarios of separation with and without a reattachment were both discussed. The roll-up vortices observed in the separated shear layer were attributed to amplification of disturbances driven by the Kelvin-Helmholtz instability. The evolution of the roll-up vortices was thought to cause boundary layer transition. In addition, the studies also discussed the effect of the separated shear layer on the frequency scaling of coherent structures.

The present work extends a previous numerical simulation study of the slat cove dynamics (Vadsola *et al.*, 2021) and focuses on a quantitative analysis using mean dynamics of an incompressible flow over a 30P30N high-lift configuration (Khorrami *et al.*, 2004). Three low Re_c are considered, namely, $Re_c = 0.832 \times 10^4$, 1.270×10^4 and 1.830×10^4. The scope of discussion is limited to the region above the airfoil where transition to turbulence occurs, and the wake region is not included at this time.

Flow configuration

The equations of conservation of mass and momentum for the incompressible flow of a Newtonian fluid are:

$$\frac{\partial u_i}{\partial x_i} = 0, \tag{1}$$

$$\frac{\partial u_i}{\partial t} + \frac{\partial}{\partial x_j} u_i u_j = -\frac{1}{\rho}\frac{\partial p}{\partial x_i} + \nu \nabla^2 u_i. \tag{2}$$

The indices i and j represent the three directions of the flow and Einstein summation notation is used. ρ and p denote fluid density and hydrodynamic pressure respectively, while u_i represents the velocity components.

These Navier-Stokes equations are solved using NEK5000 (Fischer *et al.*, 2008), an open-source code that is based upon a high-order spectral element method (Patera, 1984) and features highly scalable algorithms. A $N = 7^{th}-$order spatial accuracy is used for the present study and the temporal discretization uses a semi-implicit scheme with a $3^{rd}-$order accuracy.

Figure 1 shows the numerical setup of the computational domain with the instantaneous spanwise vorticity, $\omega_z c/U_\infty$, imposed atop for $Re_c = 1.830 \times 10^4$. Spanwise vorticity is written $\omega_z = \partial v/\partial x - \partial u/\partial y$, where x and y denote streamwise and wall-normal directions, and u and v are the corresponding instantaneous velocity components. The computational domain has a size of $x \times y \times z = 9c \times 5c \times 0.2c$ with z denoting the spanwise direction. More than 3.32×10^5 elements are employed, within each of which the solution is represented by tensor products of $7^{th}-$order polynomials in each direction [see Fig.2]. This yields a number of degrees of freedom of approximately 1.14×10^8.

The origin of the coordinate system is placed at the leading edge of the slat when flow approaches at $\alpha = 0°$. The inflow boundary (shown in red) is at a distance of $3c$ upstream of the origin where $(u, v, w) = (U_\infty \cos\alpha,\, U_\infty \sin\alpha,\, 0)$ (w signifies instantaneous velocity component in the $z-$direction) and $\alpha = 4.0°$. The outlet boundary (shown in blue) is approximately $5c$ downstream of the trailing edge of the flap where a convective boundary-condition is used. No-slip conditions are imposed on the airfoil surface, and the flow is assumed to be periodic in the $z-$direction.

Throughout the investigations, no artificial disturbances are introduced. The flow, therefore, transitions to turbulence naturally from the perturbations due to round-off or truncation errors.

Model Validation

Validation of the numerical results starts with a grid-convergence study for the highest Reynolds number considered, $Re_c = 1.830 \times 10^4$. Comparison of the results obtained using $7^{th}-$ and $9^{th}-$order polynomials, respectively, reveals minor discrepancies only in both $1^{st}-$ and $2^{nd}-$order mean

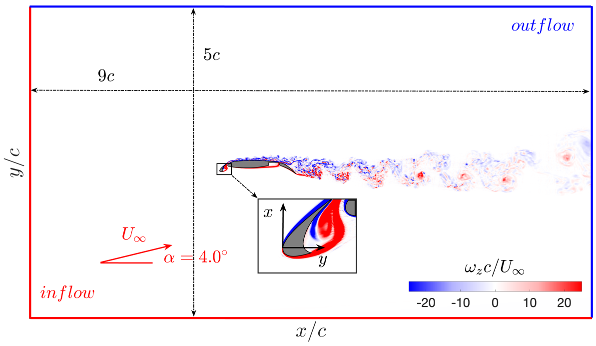

Figure 1. Sketch of the computational domain used for the calculations with instantaneous spanwise vorticity, $\omega_z c/U_\infty$, for $Re_c = 1.830 \times 10^4$ imposed on top. U_∞ and c stand for the freestream velocity and stowed chord length of the airfoil, respectively. α denotes the angle of attack.

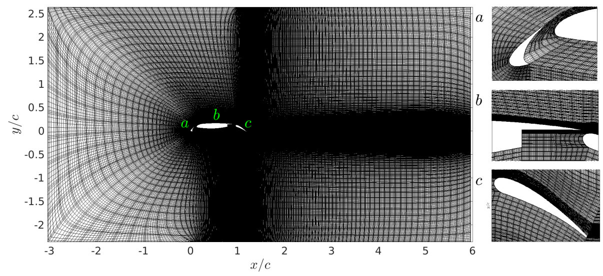

Figure 2. Grid resolution used for the domain shown in Fig. 1: (a) slat cove, (b) main element and (c) flap element.

statistics (not shown). This indicates that $7^{th}-$order polynomials are sufficient for the present study. Good agreement with the reference data (Wang & Wang, 2021*b*) is achieved in velocity magnitudes, $\langle u \rangle_{mag} = \sqrt{\langle u \rangle^2 + \langle v \rangle^2}$ ($\langle\cdot\rangle$ denotes temporal and spanwise averaging) [see Fig. 3]. Flow in the experiment, however, proceeds towards turbulence faster than in the numerical calculations. This is mostly due to the freestream turbulence intensities of the experimental flow ($\sim O(10^{-2})$ of U_∞) being substantially higher than the truncation errors ($\sim O(10^{-7})$ of U_∞).

Results

Figure 4 shows instantaneous vortical structures visualized as isosurfaces of the λ_2 criterion (Jeong & Hussain, 1995), providing an insight into the flow evolution in all Re_c cases. The flow structures are coloured by the magnitude of the streamwise velocity, u/U_∞. Different values of λ_2 are used to highlight the regional flow features at different locations. Figure 4 (a) reveals the appearance of longitudinal counter-rotating vortices shortly downstream of the main-element leading edge. These coherent structures bear qualitative similarity to those observed in flow along a concave wall where the flow is subjected to strong curvature effect (Wang *et al.*, 2018). As flow separates, a Kelvin-Helmholtz (K-H) instability takes over and leads to the formation of quasi two-dimensional (2D) rollers. Roll-up vortices propagate downstream, interacting with vortices in the wake region. An increase in Re_c yields smaller-scale structures in the wake region [see Fig. 4 (d)], and promotes the onset of quasi-2D vortices. These structures, shown in Fig. 4 (c), now appear to coexist with the longitudinal vortices as they evolve downstream into more com-

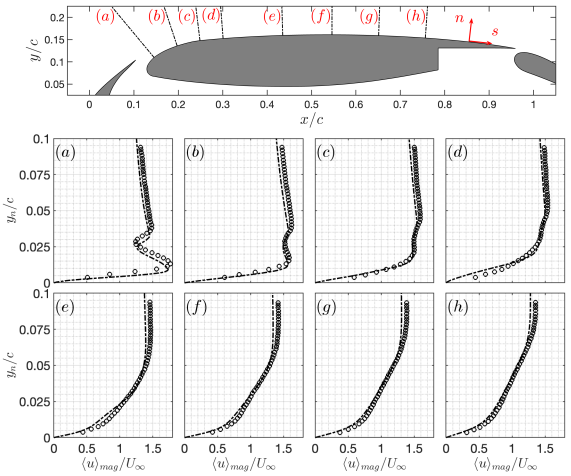

Figure 3. Comparison of velocity magnitudes, $\langle u \rangle_{mag}$, with experiments, at selected locations: $(a)-(h)$ correspond to positions $2-16$ (even numbers) in Figs. 5 and 6 of Wang & Wang (2021*b*). s and n denote directions tangential and normal to the local surface, respectively. —·— $Re_c = 1.830 \times 10^4$; ○ Wang & Wang (2021*b*).

plex structures. Longitudinal vortices are no longer perceptible as Re_c reaches $Re_c = 1.830 \times 10^4$, as shown in Fig. 4 (e). Instead, roll-up vortices appear briefly underneath the shear layer from the slat wake before the flow presents turbulent-like motions with a random distribution of hairpin vortices shortly downstream of the main-element leading edge. To identify the mechanism giving rise to the streamwise longitudinal vortices, the inviscid Rayleigh criterion is employed (not shown). It reveals a likelihood of centrifugal instability but, due to its inherent limitations (i.e. viscosity effect is not included), other criteria are required for further verification.

Figure 5 shows the mean-flow fields, $\langle u \rangle/U_\infty$, for the cases considered. The separation region over the main element reduces in size as Re_c increases and disappears for $Re_c = 1.830 \times 10^4$. For $Re_c = 0.832 \times 10^4$ and $Re_c = 1.270 \times 10^4$, the peak reverse-flow remains similar in magnitude which slightly exceeds 20.0% of U_∞. Such reverse-flow is sufficiently large to induce a local absolute instability; the boundary layer in both cases is likely globally unstable in the sense that there exists a self-sustained mode (Huerre & Monkewitz, 1990; Alam & Sandham, 2000; Theofilis, 2011; Avanci *et al.*, 2019). This requires further investigation.

Further downstream, the shear layer in all cases separates again as the flow proceeds beyond the trailing edge of the main element and does not reattach to the flap surface, forming a large wake region. The overall improvement of aerodynamic performance is seen as Re_c increases from $Re_c = 0.832 \times 10^4$ to $Re_c = 1.270 \times 10^4$ along with a corresponding reduction in the wake region, as shown in Table 1. The lift coefficient, $C_l = 2l/\rho U_\infty^2 c$, increases whereas the drag coefficient, $C_d = 2d/\rho U_\infty^2 c$, decreases (where l and d signify the lift and drag forces per unit span, respectively). Despite the further reduction in C_d as Re_c reaches $Re_c = 1.830 \times 10^4$, there is an unexpected decrease in C_l. It is conjectured that the separation region modifies the curvature of the external flow, and thus the effective camber shape, leading to a decrease in C_l in cases where separation does not exist. As expected, the pressure drag contribution decreases significantly as the Reynolds number increases and the wake region narrows. And the lift to drag ratio increases significantly as the Reynolds number

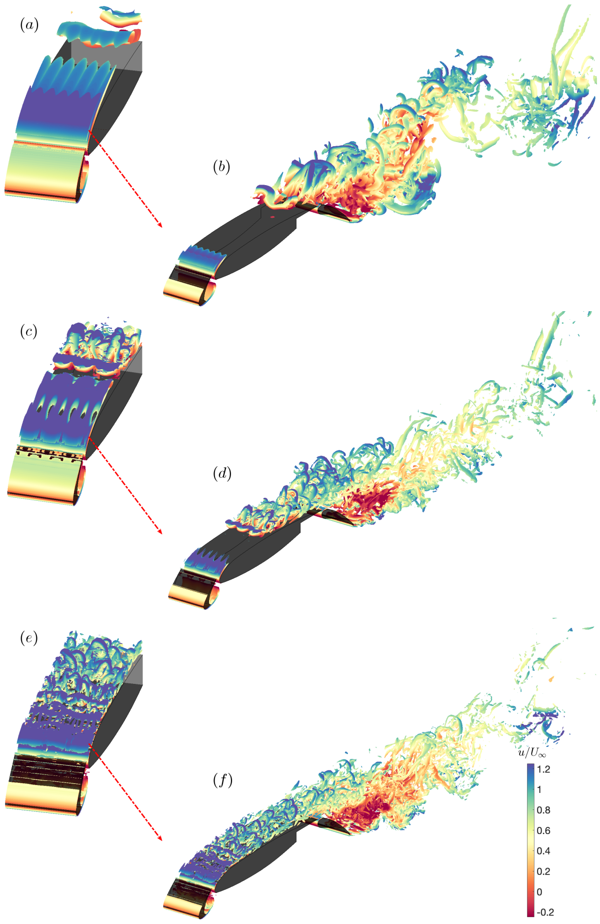

Figure 4. Iso-surfaces of the λ_2 (the middle eigenvalue of the strain-rate tensor), coloured by the magnitude of streamwise velocity, u/U_∞. $(a,\ b)$: $\underline{Re_c = 0.832 \times 10^4}$ at $tU_\infty/c = 10.80$ (t denotes time); (a) $\lambda_2 = -10.0$ and (b) $\lambda_2 = -50.0$. $(c,\ d)$: $\underline{Re_c = 1.270 \times 10^4}$ at $tU_\infty/c = 23.70$; (c) $\lambda_2 = -50.0$ and (d) $\lambda_2 = -100.0$. $(e,\ f)$: $\underline{Re_c = 1.830 \times 10^4}$ at $tU_\infty/c = 23.88$; (e) $\lambda_2 = -100.0$, (f) $\lambda_2 = -150.0$.

Table 1. Summary of aerodynamic coefficients. Re_c denotes chordwise Reynolds number; C_l and C_d denote lift and drag coefficients, respectively. C_{d_p} represents contribution of pressure drag.

$Re_c(\times 10^4)$	C_l	C_d	$C_{d_p}(\%)$	C_l/C_d
0.832	1.519	0.104	83.2	14.5
1.270	1.575	0.0592	73.1	26.6
1.830	1.436	0.0560	65.3	25.6

increases from $Re_c = 0.832 \times 10^4$ to $Re_c = 1.270 \times 10^4$, but decreases slightly at the highest Reynolds number since the lift is reduced in this case.

Figure 6 presents the distribution of the pressure coefficient, $C_p = -2(\langle p \rangle - p_\infty)/\rho U_\infty^2$ (p_∞ denotes the freestream pressure). The impact of Re_c on C_p is most pronounced above the main element. One salient feature of a boundary-layer separation is its quasi constant-pressure region shortly downstream of the separation point (Carmichael, 1981), as observed for $Re_c = 0.8320 \times 10^4$ and $Re_c = 1.270 \times 10^4$ in the figure. Above the flap, the absence of a reattachment to the surface

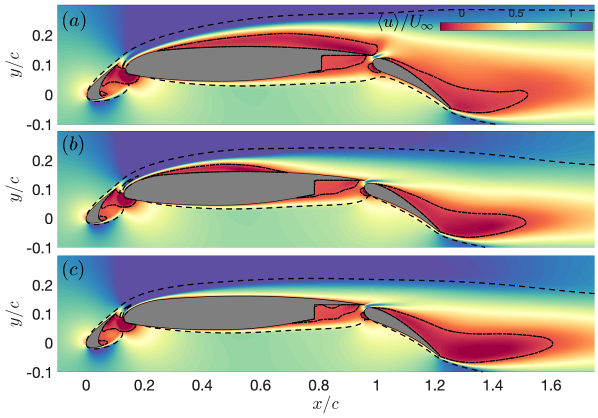

Figure 5. Mean-flow fields, $\langle u \rangle / U_\infty$: ($a$) $Re_c = 0.832 \times 10^4$, (b) $Re_c = 1.270 \times 10^4$, and (c) $Re_c = 1.830 \times 10^4$. — — — δ_{99} (boundary-layer thickness); —·— $\langle u \rangle = 0.0$.

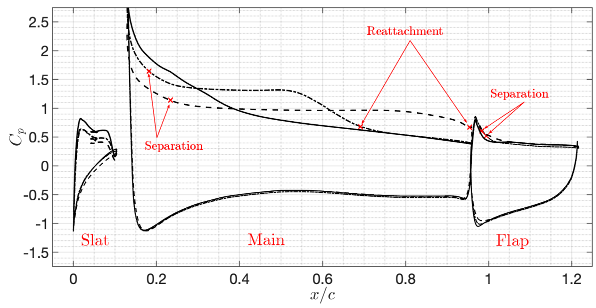

Figure 6. Profiles of pressure coefficients, C_p, for the cases considered. — — — $Re_c = 0.832 \times 10^4$; —·— $Re_c = 1.270 \times 10^4$; ——— $Re_c = 1.830 \times 10^4$.

is reflected by a constant-pressure region that extends to the trailing edge. An increase in pressure following the constant-pressure region that signifies transition in the separated shear layer is not observed as documented in the literature (Yarusevych *et al.*, 2006).

Figure 7 shows the Reynolds shear stress, $-\langle u'v' \rangle$, over the first half of the airfoil. A switch in sign is observed over the main element that shifts progressively upstream as Re_c increases. This switch partially reflects the motions of the v component as flow evolves downstream, going from upwards to downwards. This location also appears to match where roll-up vortices start to occur above the main element in all cases [see Fig. 4]. Downstream of the slat cove, a pronounced switch is also observed, particularly in the $Re_c = 1.830 \times 10^4$ case. This is mostly due to reverse motion of the u component in the recirculation region. Figure 8 presents the Reynolds normal stresses on the suction side of the entire airfoil. Turbulent kinetic energy (TKE), $\mathscr{K} = \frac{1}{2}\langle u_i' u_i' \rangle$, is intensified aft of the separation bubble for both $Re_c = 0.832 \times 10^4$ and $Re_c = 1.270 \times 10^4$, where both $\langle u'u' \rangle$ and $\langle v'v' \rangle$ contribute significantly to the total. For $Re_c = 1.830 \times 10^4$, however, $\frac{1}{2}\langle u_i' u_i' \rangle$ is attenuated substantially, the majority of which comes from $\langle u'u' \rangle$ only.

The transport equation of the TKE is given by (Pope, 2000):

$$\frac{\partial \mathscr{K}}{\partial t} + \underbrace{\frac{\partial}{\partial x_k}(\langle u_k \rangle \mathscr{K})}_{C} = \underbrace{-\langle u_i' u_k' \rangle \frac{\partial \langle u_i \rangle}{\partial x_k}}_{P} \underbrace{- \frac{1}{2}\frac{\partial}{\partial x_k}\langle u_i' u_i' u_k' \rangle}_{T^t} \qquad (3)$$
$$\underbrace{- \frac{1}{\rho}\frac{\partial}{\partial x_k}\langle p' u_k' \rangle}_{\Pi^t} \underbrace{- \nu \left\langle \frac{\partial u_i'}{\partial x_k}\frac{\partial u_i'}{\partial x_k} \right\rangle}_{\varepsilon} + \underbrace{\nu \nabla^2 \mathscr{K}}_{D},$$

where C denotes the convection, P the production, T^t the turbulent transport, Π^t the pressure diffusion, ε the pseudo-dissipation, and D the viscous diffusion. Contours of the budget terms for the considered cases, scaled using ν and U_∞, are shown in Fig. 9. Despite the differences in locations where the various budgets terms are intensified, changing Re_c does not modify the overall characteristics of the budget qualitatively: a major balance is reached among the P, C, ε and $\Pi^t + T^t$ terms; D is negligible regardless of the Re_c. The size of the separation region appears to affect the energy transfer: the larger the size, the more the energy is transferred from the mean flow to the fluctuations. The pronounced promotion in energy transfer is likely due to the $K-H$ instability mechanism at play, which acts as a local amplifier driving the growth of the perturbations along the inflection point, $\partial^2 \langle u \rangle / \partial y^2 = 0$ (Teng & Piomelli, 2022).

Summary

The present study presents the transitional behaviour of an incompressible flow past a 30P30N high-lift airfoil from the perspective of mean-statistics. Investigations include three low Re_c: $Re_c = 0.832 \times 10^4$, 1.270×10^4 and 1.830×10^4. The angle of attack is fixed at 4.0 degrees. A series of well-resolved DNS is implemented via a high-order spectral element method. Good agreement with experimental measurements is achieved as shown through velocity magnitude profiles along the main element of the airfoil. The present study reveals several interesting phenomena. Pairs of longitudinal counter-rotating vortices are observed. The inviscid Rayleigh criterion indicates a likelihood of centrifugal instability for such coherent structures, while other criteria will be investigated in the future for verification. Despite the expected decrease in drag force, an unusual decrease in lift is observed in going from the middle to the highest Re_c case. It is conjectured that the separation region modifies the effective camber shape of the airfoil and, consequently, leads to a promotion in lift for the two lower Reynolds number cases. As the separation region is eliminated in the highest Reynolds number case, the lift decreases relative to that of the previous (middle) Reynolds number case. This requires further investigation. A switch in sign of Reynolds shear stress is observed over the main element in all cases. Such a switch seemingly corresponds to the spot where the formations of roll-up vortices occur above the main element. Attenuation of the turbulent kinetic energy (TKE) is pronounced on the suction side for the highest Re_c case, whereas the other two lower Re_c cases present more intensified TKE. An analysis of the TKE budget reveals that, despite the differences in Re_c considered, the overall characteristics of the budget remain qualitatively the same. In future work, we will investigate the reported phenomena in more detail and in the meantime we employ a dynamic analysis to complement the current exploration.

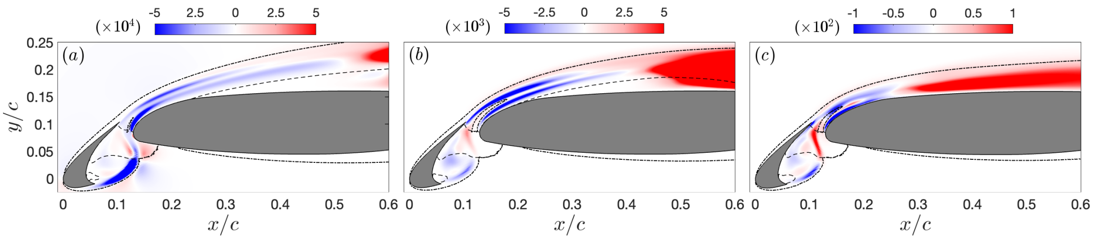

Figure 7. Reynolds shear stresses, $-\langle u'v'\rangle/U_\infty^2$, over the first half of the airfoil. (a) $Re_c = 0.832\times10^4$ (scale multiplied by a factor of 10^4), (b) $Re_c = 1.270\times10^4$ (scale multiplied by a factor of 10^3) and (c) $Re_c = 1.830\times10^4$ (scale multiplied by a factor of 10^2). —·— δ_{99}; – – – $\langle u\rangle = 0.0$.

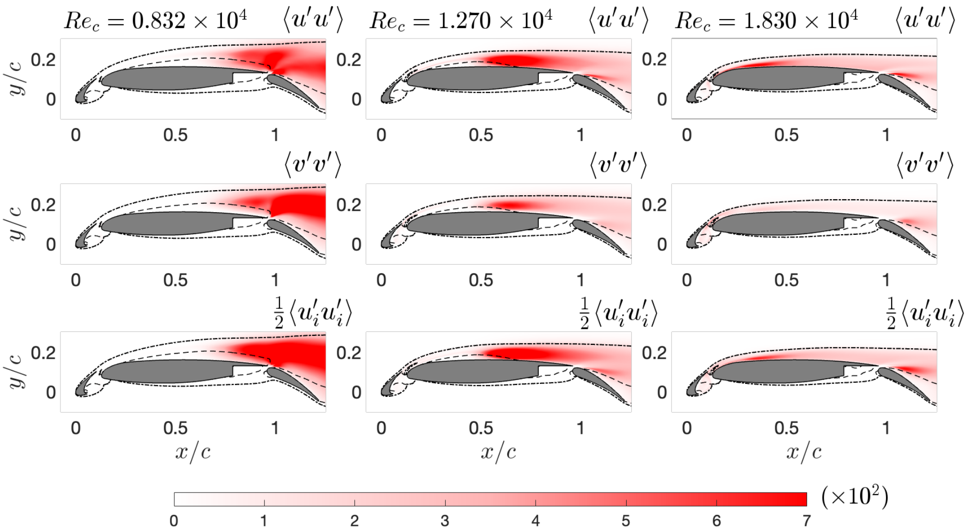

Figure 8. Reynolds normal stresses on the upper side of the airfoil (normalised by U_∞^2). —·— δ_{99}; – – – $\langle u\rangle = 0.0$. Scales are multiplied by a factor of 10^2 for all cases.

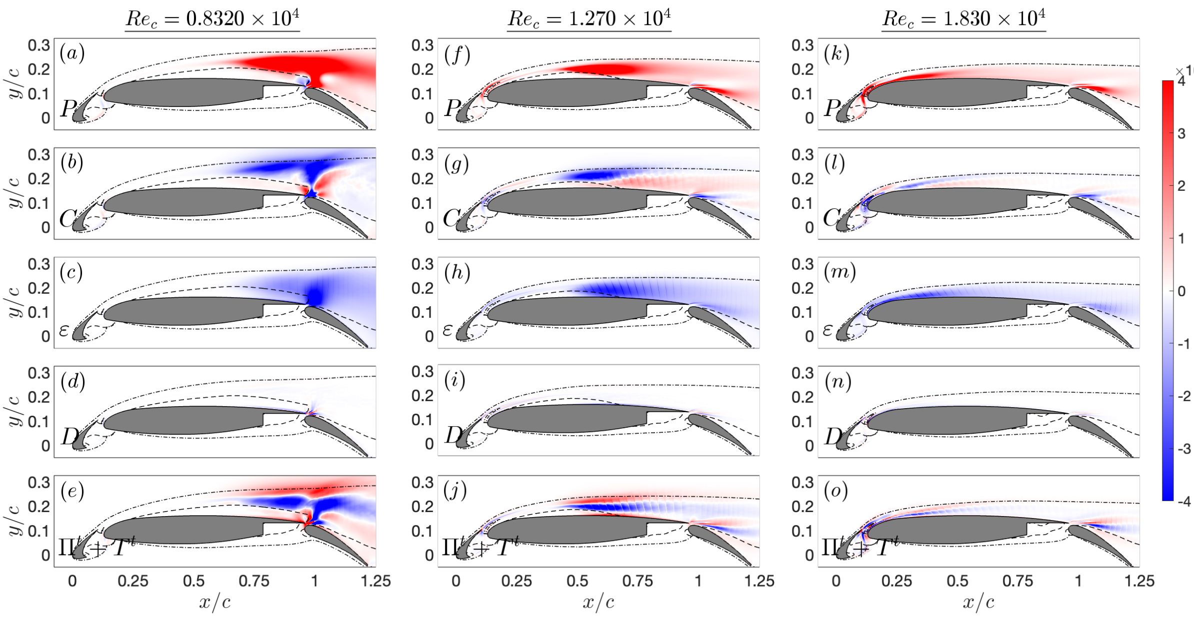

Figure 9. Budget terms of turbulent kinetic energy, $\mathscr{K}$, for the cases considered. P denotes the production, C the convection, ε the pseudo-dissipation, D the viscous diffusion, Π^t the pressure diffusion, and T^t the turbulent transport (terms shown are scaled using ν and U_∞). —·— δ_{99}; – – – $\langle u\rangle = 0.0$.

REFERENCES

Alam, M. & Sandham, N. D. 2000 Direct numerical simulation of 'short' laminar separation-bubbles with turbulent reattachment. *Journal of Fluid Mechanics* **410**, 1–28.

Avanci, M. P., Rodríguez, D. & A., Leonardo, S. de B. 2019 A geometrical criterion for absolute instability in separated boundary-layers. *Physics of Fluids* **31** (1), 014103.

Carmichael, B. H. 1981 Low Reynolds number airfoil survey. Technical report. NASA Langley Research Center.

Fischer, P. F., Lottes, J. W. & Kerkemeier, S. G. 2008 NEK5000 webpage. "http://nek5000.mcs.anl.gov".

Huerre, P. & Monkewitz, P. A. 1990 Local and global instabilities in spatially developing flows. *Annual Review of Fluid Mechanics* **22** (1), 473–537.

Jeong, J. & Hussain, F. 1995 On the identification of a vortex. *Journal of Fluid Mechanics* **285**, 69–94.

Khorrami, M., Choudhari, M. & Jenkins, L. 2004 Characterization of unsteady flow structures near leading-edge slat: Part II: 2D Computations. In *10th AIAA/CEAS Aeroacoustics Conference*, p. 2802.

Lissaman, P. B. S. 1983 Low-Reynolds-number airfoils. *Annual Review of Fluid Mechanics* **15** (1), 223–239.

Patera, A. T. 1984 A spectral element method for fluid dynamics: Laminar flow in a channel expansion. *Journal of Computational Physics* **54** (3), 468–488.

Pope, S. B. 2000 *Turbulent Flows*. Cambridge University Press.

Teng, M. & Piomelli, U. 2022 Instability and transition of a boundary layer over a backward-facing step. *Fluids* **7** (1), 35.

Theofilis, V. 2011 Global linear instability. *Annual Review of Fluid Mechanics* **43**, 319–352.

Vadsola, M., Agbaglah, G. G. & Mavriplis, C. 2021 Slat cove dynamics of low Reynolds number flow past a 30P30N high lift configuration. *Physics of Fluids* **33** (3).

Wang, J. S., Feng, L. H., Wang, J. J. & Li, T. 2018 Görtler vortices in low-Reynolds-number flow over multi-element airfoil. *Journal of Fluid Mechanics* **835**, 898–935.

Wang, J. S. & Wang, J. J. 2021*a* Vortex dynamics for flow around the slat cove at low Reynolds numbers. *Journal of Fluid Mechanics* **919**, A27.

Wang, J. S. & Wang, J. J. 2021*b* Wake-induced transition in the low-Reynolds-number flow over a multi-element airfoil. *Journal of Fluid Mechanics* **915**, A28.

Wang, J. S., Wang, J. J. & Kim, K. C. 2019 Wake/shear layer interaction for low-Reynolds-number flow over multi-element airfoil. *Experiments in Fluids* **60**, 1–24.

Yarusevych, S., Sullivan, P. E. & Kawall, J. G. 2006 Coherent structures in an airfoil boundary layer and wake at low Reynolds numbers. *Physics of Fluids* **18** (4).

Yarusevych, S., Sullivan, P. E. & Kawall, J. G. 2009 On vortex shedding from an airfoil in low-Reynolds-number flows. *Journal of Fluid Mechanics* **632**, 245–271.